Research Article | Vol. 26, No. 14 | 9 Jul 2018 | OPTICS EXPRESS 18423
Optics EXPRESS

Phase-resolved terahertz self-detection near-field microscopy

MARIA C. GIORDANO,[1] STEFAN MASTEL,[2] CLEMENS LIEWALD,[3,4] LORENZO L. COLUMBO,[5,6] MASSIMO BRAMBILLA,[5,7] LEONARDO VITI,[1] ANTONIO POLITANO,[8] KAI ZHANG,[9] LIANHE LI,[10] A. GILES DAVIES,[10] EDMUND H. LINFIELD,[10] RAINER HILLENBRAND,[11,12] FRITZ KEILMANN,[3] GAETANO SCAMARCIO,[5,7,*] AND MIRIAM S. VITIELLO[1]

[1]*NEST, CNR - Istituto Nanoscienze and Scuola Normale Superiore, Piazza San Silvestro 12, I-56127 Pisa, Italy*
[2]*CIC nanoGUNE Consolider, 20018 Donostia—San Sebastian, Spain*
[3]*Fakultät für Physik & Center for NanoScience (CeNS), Ludwig-Maximilians-Universität München, Geschwister-Scholl-Platz 1, 80539 Munich, Germany*
[4]*Nanosystems Initiative Munich, Schellingstrasse 4, 80799 Munich, Germany*
[5]*CNR- Istituto di Fotonica e Nanotecnologie, Sede di Bari, via Amendola 173, I-70126 Bari, Italy*
[6]*Dipartimento di Elettronica e Telecomunicazioni, Politecnico di Torino, Corso Duca degli Abruzzi 24, 10129 Torino, Italy*
[7]*Dipartimento Interateneo di Fisica, Università degli Studi e Politecnico di Bari, via Amendola 173, I-70126 Bari, Italy*
[8]*Fondazione Istituto Italiano di Tecnologia, Graphene Labs, via Morego 30, 16163, Genova, Italy*
[9]*i-Lab, Suzhou Institute of Nano-Tech and Nano-Bionics, Chinese Academy of Sciences, Suzhou, Jiangsu, China*
[10]*School of Electronic and Electrical Engineering, University of Leeds, Leeds LS2 9JT, UK*
[11]*IKERBASQUE, Basque Foundation for Science, 48013 Bilbao, Spain*
[12]*CIC nanoGUNE and UPV/EHU, 20018 Donostia-San Sebastian, Spain*
[*]*gaetano.scamarcio@uniba.it*

Abstract: At terahertz (THz) frequencies, scattering-type scanning near-field optical microscopy (s-SNOM) based on continuous wave sources mostly relies on cryogenic and bulky detectors, which represents a major constraint for its practical application. Here, we devise a THz s-SNOM system that provides both amplitude and phase contrast and achieves nanoscale (60-70nm) in-plane spatial resolution. It features a quantum cascade laser that simultaneously emits THz frequency light and senses the backscattered optical field through a voltage modulation induced inherently through the self-mixing technique. We demonstrate its performance by probing a phonon-polariton-resonant CsBr crystal and doped black phosphorus flakes.

OCIS codes: (180.4243) Near-field microscopy; (180.5810) Scanning microscopy; (140.5965) Semiconductor lasers, quantum cascade; (110.6795) Terahertz imaging; (110.3175) Interferometric imaging; (310.6628) Subwavelength structures, nanostructures.

References and links

1. F. Keilmann and R. Hillenbrand, "Near-Field Nanoscopy by Elastic Light Scattering from a Tip", in Nano-Optics and Near-Field Optical Microscopy, Zayats, & A. D. Richards, eds., Artech House, Boston, London (2009).
2. A. J. Huber, F. Keilmann, J. Wittborn, J. Aizpurua, and R. Hillenbrand, "Terahertz Near-Field Nanoscopy of Mobile Carriers in Single Semiconductor Nanodevices," Nano Lett. **8**(11), 3766–3770 (2008).
3. R. Hillenbrand and F. Keilmann, "Complex Optical Constants on a Subwavelength Scale," Phys. Rev. Lett. **85**(14), 3029–3032 (2000).
4. N. Ocelic, A. Huber, and R. Hillenbrand, "Pseudo-heterodyne Detection for Background-Free Near-Field Spectroscopy," Appl. Phys. Lett. **89**(10), 101124 (2006).
5. H. G. von Ribbeck, M. Brehm, D. W. van der Weide, S. Winnerl, O. Drachenko, M. Helm, and F. Keilmann, "Spectroscopic THz near-field microscope," Opt. Express **16**(5), 3430–3438 (2008).

#325050 https://doi.org/10.1364/OE.26.018423
Journal © 2018 Received 28 Feb 2018; revised 26 May 2018; accepted 30 May 2018; published 3 Jul 2018

Optics EXPRESS

6. H.-T. Chen, S. Kraatz, G. C. Cho, and R. Kersting, "Identification of a resonant imaging process in apertureless near-field microscopy," Phys. Rev. Lett. **93**(26), 267401 (2004).
7. C. Liewald, S. Mastel, J. Hesler, A. J. Huber, R. Hillenbrand, and F. Keilmann, "All-electronic terahertz nanoscopy," Optica **5**(2), 159 (2018).
8. A. J. L. Adam, "Review of Near-Field Terahertz Measurement Methods and Their Applications," J. Infrared Millim. Terahertz Waves **32**(8-9), 976–1019 (2011).
9. W. L. Chan, J. Deibel, and D. M. Mittleman, "Imaging with terahertz radiation," Rep. Prog. Phys. **70**(8), 1325–1379 (2007).
10. P. Dean, O. Mitrofanov, J. Keeley, I. Kundu, L. Li, E. H. Linfield, and A. Giles Davies, "Apertureless near-field THz imaging using the self-mixing effect in a quantum cascade laser," Appl. Phys. Lett. **108**(9), 091113 (2016).
11. R. Degl'Innocenti, R. Wallis, B. Wei, L. Xiao, S. J. Kindness, O. Mitrofanov, P. Braeuninger-Weimer, S. Hofmann, H. E. Beere, and D. A. Ritchie, "Terahertz nanoscopy of plasmonic resonances with a quantum cascade laser," ACS Photonics **4**(9), 2150–2157 (2017).
12. T. Taimre, K. Bertling, Y. L. Lim, P. Dean, D. Indjin, and A. D. Rakić, "Methodology for materials analysis using swept-frequency feedback interferometry with terahertz frequency quantum cascade lasers," Opt. Express **22**(15), 18633–18647 (2014).
13. M. S. Vitiello, G. Scalari, B. S. Williams, and P. De Natale, "Quantum cascade lasers: 20 years of challenges," Opt. Express **23**(4), 8462–8475 (2015).
14. G. Giuliani and S. Donati, "Laser interferometry", in Unlocking Dynamical Diversity, John Wiley & Sons, Ltd, pp. 217–255 (2005).
15. T. Taimre, M. Nikolić, K. Bertling, Y. L. Lim, T. Bosch, and A. D. Rakić, "Laser feedback interferometry: a tutorial on the self-mixing effect for coherent sensing," Adv. Opt. Photonics **7**(3), 570–631 (2015).
16. F. P. Mezzapesa, L. L. Columbo, M. Brambilla, M. Dabbicco, S. Borri, M. S. Vitiello, H. E. Beere, D. A. Ritchie, and G. Scamarcio, "Intrinsic stability of quantum cascade lasers against optical feedback," Opt. Express **21**(11), 13748–13757 (2013).
17. F. P. Mezzapesa, L. L. Columbo, C. Rizza, M. Brambilla, A. Ciattoni, M. Dabbicco, M. S. Vitiello, and G. Scamarcio, "Photo-generated metamaterials induce modulation of CW terahertz quantum cascade lasers," Sci. Rep. **5**(1), 16207 (2015).
18. F. P. Mezzapesa, L. L. Columbo, M. Brambilla, M. Dabbicco, M. S. Vitiello, and G. Scamarcio, "Imaging of free carriers in semiconductors via optical feedback in terahertz quantum cascade lasers," Appl. Phys. Lett. **104**(4), 041112 (2014).
19. R. Lang and K. Kobayashi, "External optical feedback effects on semiconductor injection laser properties," IEEE J. Quantum Electron. **16**(3), 347–355 (1980).
20. T. G. Fiske and L. B. Coleman, "Longitudinal-optical phonons in thin films of rubidium iodide, potassium iodide, rubidium bromide, cesium iodide, and cesium bromide," Phys. Rev. B Condens. Matter **45**(3), 1414–1424 (1992).
21. T. Taubner, F. Keilmann, and R. Hillenbrand, "Nanomechanical Resonance Tuning and Phase Effects in Optical Near-Field Interaction," Nano Lett. **4**(9), 1669–1672 (2004).
22. L. Viti, J. Hu, D. Coquillat, A. Politano, C. Consejo, W. Knap, and M. S. Vitiello, "Heterostructured hBN-BP-hBN Nanodetectors at Terahertz Frequencies," Adv. Mater. **28**(34), 7390–7396 (2016).
23. L. Viti, J. Hu, D. Coquillat, W. Knap, A. Tredicucci, A. Politano, and M. S. Vitiello, "Black Phosphorus Terahertz Photodetectors," Adv. Mater. **27**(37), 5567–5572 (2015).
24. O. Mitrofanov, L. Viti, E. Dardanis, M. C. Giordano, D. Ercolani, A. Politano, L. Sorba, and M. S. Vitiello, "Near-field terahertz probes with room-temperature nanodetectors for subwavelength resolution imaging," Sci. Rep. **7**, 44240 (2017).
25. M. A. Huber, F. Mooshammer, M. Plankl, L. Viti, F. Sandner, L. Z. Kastner, T. Frank, J. Fabian, M. S. Vitiello, T. L. Cocker, and R. Huber, "Femtosecond photo-switching of interface polaritons in black phosphorus heterostructures," Nat. Nanotechnol. **12**, 207 (2017).
26. M. S. Vitiello and L. Viti, "Photonic Devices Based On Black-Phosphorus and Combined Hybrid 2D nanomaterials," Riv. Nuovo Cim. **39**, 371–398 (2016).
27. J. Abate, S. Gamage, Z. Li, V. Babicheva, M. H. Javani, H. Wang, S. B. Cronin, and M. I. Stockman, "Nanoscopy reveals surface-metallic black phosphorus," Light Sci. Appl. **5**(10), e16162 (2016).
28. Y. Xu, J. Yuan, L. Fei, X. Wang, Q. Bao, Y. Wang, K. Zhang, and Y. Zhang, "Selenium-Doped Black Phosphorus for High-Responsivity 2D Photodetectors," Small **12**(36), 5000–5007 (2016).
29. F. Xia, H. Wang, and Y. Jia, "Rediscovering black phosphorus as an anisotropic layered material for optoelectronics and electronics," Nat. Commun. **5**(1), 4458 (2014).
30. M. S. Vitiello and A. Tredicucci, "Tunable emission in Terahertz quantum cascade lasers," IEEE Trans. Terahertz Sci. Technol. **1**(1), 76–84 (2011).
31. D. Burgoff, T.-Y. Kao, N. Han, C. W. I. Chan, X. Cai, Y. Yang, D. J. Hayton, J.-R. Gao, J. L. Reno, and Q. Hu, "Terahertz laser frequency combs," Nat. Photonics **8**(6), 462–467 (2014).
32. M. Rosch, G. Scalari, M. Beck, and J. Faist, "Octave spanning semiconductor laser," Nat. Photonics **9**(1), 42–47 (2015).
33. N. Rotenberg and L. Kuipers, "Mapping nanoscale light fields," Nat. Photonics **8**(12), 919–926 (2014).
34. S. Amarie and F. Keilmann, "Broadband-infrared assessment of phonon resonance in scattering-type near-field microscopy," Phys. Rev. B **83**(4), 045404 (2011).

Optics EXPRESS

35. L. L. Columbo and M. Brambilla, "Multimode regimes in quantum cascade lasers with optical feedback," Opt. Express **22**(9), 10105–10118 (2014).
36. M. S. Vitiello, L. Consolino, S. Bartalini, A. Taschin, A. Tredicucci, M. Inguscio, and P. De Natale, "Quantum limited frequency fluctuations in a terahertz laser," Nat. Photonics **6**(8), 525–528 (2012).
37. M. Ravaro, S. Barbieri, G. Santarelli, V. Jagtap, C. Manquest, C. Sirtori, S. P. Khanna, and E. H. Linfield, "Measurement of the intrinsic linewidth of terahertz quantum cascade lasers using a near-infrared frequency comb," Opt. Express **20**(23), 25654–25661 (2012).

1. Introduction

Terahertz (THz) frequency electromagnetic waves (30–300 μm wavelength) can resonantly interact with fundamental excitations of molecules and solids and thus offer an ideal tool for the optical characterization of emerging low-dimensional materials and biological-systems. Scattering-type scanning near-field optical microscopy (s-SNOM) displayed an exceptional potential for nanoscale imaging of material properties [1] as has been demonstrated also at 2.5 THz [2]. In s-SNOM, an incident light beam is focused on a sharp atomic force microscope (AFM) metallic tip strongly confining the radiation to the near-field region of its nanometric apex. Nanoscale resolved (10 - 100 nm) optical images can be retrieved by analyzing the scattered radiation as a function of tip position, placing the tip in close proximity to the sample surface.

Coherent imaging, i.e. detection of amplitude and phase contrast, is crucial to get information on the real and imaginary parts of the dielectric response and hence several interferometric approaches have been developed allowing amplitude and phase resolved s-SNOM imaging in the visible and infrared spectral ranges [3, 4]. Solutions based on fs pulsed laser sources and electro-optic sampling detection in the THz range [5, 6] or solutions based on microwave circuitry in the sub-THz range [7] have been reported. However, in spite of a strong demand to extend in the far-infrared the spectral coverage of coherent nano-imaging based on *continuous-wave (CW) compact sources*, conventional interferometric techniques [2, 8, 9] have suffered from the poor dynamic range of cryogenically cooled bolometric detectors needed to measure the typically small s-SNOM signals [2]. Progress in coherent THz nano-imaging would therefore greatly benefit from compact, room-temperature operating and fast detection systems for THz frequency operation.

Here we tackle the problem by conceiving a simple, potentially fast and compact s-SNOM system based on a THz quantum cascade laser (QCL) operated CW in the self-detection (SD) mode. A similar approach has been recently exploited to produce THz images with sub-wavelength spatial resolution [10, 11]. In this work, we demonstrate amplitude- and phase-resolved background-free SD-s-SNOM imaging with 60-70 nm spatial resolution comparable to the scattering tip size, providing a key step forward to make THz nanoscopy a widely used tool. Our approach, based on a simple 2-parameter fitting of self-mixing interferograms, outperforms by far all previously reported attempts based on the use of self-mixing and either attaining incoherent near-field s-SNOM imaging, or using a rather complex 6-parameter fitting procedure for amplitude-like and phase-like images at diffraction-limited resolutions (> 100 μm) [12].

2. Results and discussion

2.1 The general concept of SD-s-SNOM

In our experimental configuration, we use the radiation source, a THz quantum cascade laser (QCL) [13], (see Experimental Methods) not only for illuminating the tip but also for detecting the radiation field scattered from the tip, therefore avoiding the use of bulky THz cryogenic detectors. The near-field scattering is measured through the voltage change (ΔV) across the electrical contacts of the THz QCL, induced by the self-mixing effect [14, 15]. This effect is based on the reinjection of a small fraction (10^{-4} 10^{-2}) of the emitted field that coherently interferes within the laser cavity.

Optics EXPRESS

The inherent stability of QCLs against optical feedback [16] has been recently exploited in a number of self-mixing interferometry (SMI) configurations, providing an interesting method to control the emission of THz QCLs by reconfigurable photo-generated anisotropic metamaterials [17], to trace the free carrier distribution in a semiconductor target [18], and to map the real and imaginary refractive index of polymeric materials [12], for example.

In our system (Fig. 1(a)), the 2.7 THz QCL radiation is focused onto the apex of a Pt tip, which is sinusoidally dithered, normally and in close proximity to the sample surface at frequency Ω. The scattered field E_s is collected by a parabolic mirror and focused back onto the QCL front facet along the same incident optical path, inducing the changes in the QCL voltage (ΔV) (see details on the experimental arrangement in Appendix 1). Hence, ΔV measures the optical response of the sample. To quantify this properly, we relied on the well-established Lang-Kobayashi (LK) model [19], and extended it to encompass a complex sample permittivity. In the very weak feedback limit, the voltage change at the QCL terminals can be written (see Appendix 2):

$$\Delta V \propto s\cos(\omega_0 \frac{2L}{c} - \varphi) \tag{1}$$

where s and φ are the amplitude and phase, respectively, of the ratio between scattered and incident electrical fields of THz radiation, $\omega_0 = 2\pi c/\lambda$ is the unperturbed laser frequency, and L is the laser-to-tip distance which varies by the tip dithering and by the piezoelectric mirror (PZM) displacement. By using an optical attenuator (A), the feedback remains sufficiently low to keep the system in the validity range of Eq. (1). In this regime, the proposed experimental layout is similar to a single-arm homodyne interferometer [14], in which the laser output facet and the tip define the external cavity of our self-mixing interferometer.

Equation (1) contains all necessary physical quantities to predict observable amplitude and phase contrasts in SD-s-SNOM images. Although in conventional s-SNOM, the phase contrast is extracted by analyzing the detector signal variations induced by changing the optical path length of the reference beam of an interferometer, in SD-s-SNOM the amplitude and phase information is obtained from the analysis of the ΔV as a function of ΔL as explained below.

Optics EXPRESS

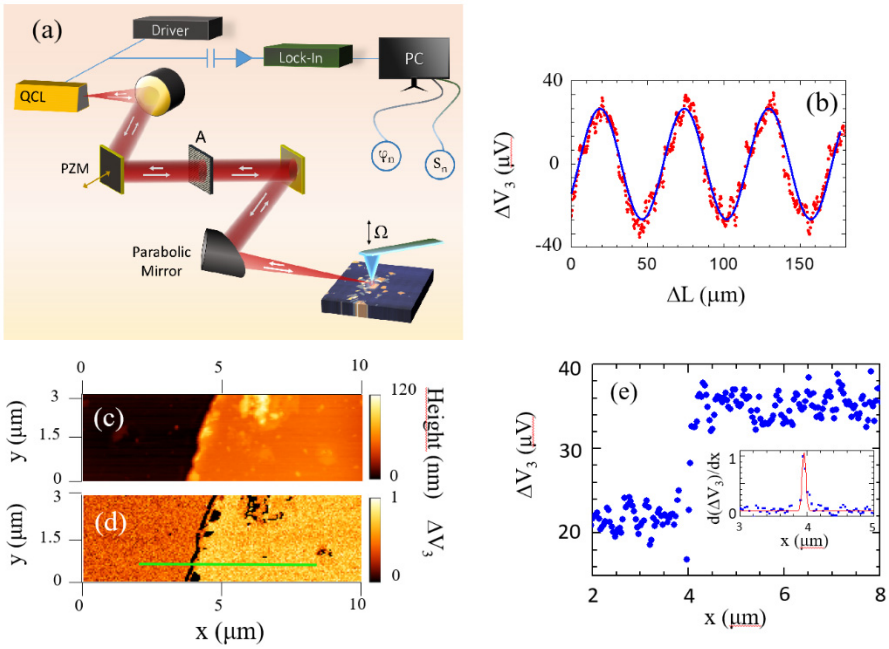

Fig. 1. Self-detection scattering type near field optical microscope with nanometer resolution at terahertz frequencies. (a) Schematic diagram showing the experimental arrangements. The same optical components (two paraboloid mirrors, an attenuator (A), one fixed mirror and one piezo-actuated mirror (PZM)) focus the THz beam emitted by the QCL onto the apex of a Pt tip sinusoidally dithered at frequency Ω in close proximity to the sample surface and feeds the scattered radiation back into the QCL cavity to produce self-mixing. The distance $L \approx 60$ cm between the QCL front facet and the tip can be varied by translating the PZM. (b) Self-mixing induced modulation from a Au surface of the voltage drop across the QCL obtained using the experimental arrangement (a) and measured by a lock-in amplifier to the $n = 3$ demodulation order, as a function of ΔL. The dots are the experimental data and the solid line is the best-fitted curve obtained using Eq. (2). The ΔV_3 signal show the expected $\lambda/2$ periodicity characteristic of self-mixing. (c) AFM topographic and (d) 3rd harmonic near-field THz imaging of the Au-on-silicon sample at a fixed mirror position. (e) Edge response profile extracted from (d) by averaging seven adjacent rows of pixels along the green horizontal line. The inset shows the corresponding spatial derivative, which has been fitted by a Gaussian function (red curve) with a full-width-at-half-maximum of 65 nm.

2.2 The implementation of SD-s-SNOM

In our arrangement, as is typical in s-SNOM for effectively distinguishing the near-field scattering from background scattering [1], ΔV is demodulated at low-order harmonics of the dither frequency using a lock-in amplifier, and the measured harmonic amplitudes ΔV_n are recorded up to the order $n = 5$ as a function of the displacement ΔL. Decomposing ΔV into harmonic components $\Delta V = \sum_{n=0}^{+\infty} \Delta V_n \cos(n\Omega t)$, we show that the demodulated signals equivalently carry information on the optical amplitude and phase components s_n and φ_n (see Appendix 2):

$$\Delta V_n \propto s_n \cos(\omega_0 \frac{2L(t)}{c} - \varphi_n) \qquad (2)$$

The experimental ΔV_n *vs* ΔL curves (e.g. ΔV_3 in Fig. 1(b)) demonstrates that our SD-s-SNOM system behaves similarly to an external interferometer and produces approximately

Optics EXPRESS

sinusoidal interference fringes, as predicted by Eq. (2). Figures 1(c)-(d) provide direct proof that the SD-s-SNOM signal is sufficiently stable for homodyne THz imaging.

2.3 Deep sub-wavelength in-plane spatial resolution

Comparison between the AFM (Fig. 1(c)) and the self-detected (Fig. 1(d)) images of a gold film deposited on a SiO_2-coated silicon substrate demonstrates the capability of our THz imaging system to achieve an in-plane resolution comparable with the employed tip apex sizes (50-70nm). Figure 1(e) shows the ΔV_3 signal collected along the green horizontal line in panel 1d traversing the edge of the gold-coated region. The inset of Fig. 1(e) shows the corresponding first-order spatial derivative. From the full-width-at-half-maximum of the Gaussian curve interpolating the derivative function (red curve in the inset of Fig. 1(e)), we can retrieve a remarkable spatial resolution of σ_x = 68 nm along the horizontal (fast) axis, corresponding to ~λ/1500.

2.4 Amplitude and phase contrast imaging capability

The phase-contrast at THz frequencies between gold and SiO_2 is negligibly small, as is usual for all combinations of non-resonant materials [9]. Hence, to provide a proof-of-principle of the amplitude and phase contrast imaging capability of the SD-s-SNOM, we selected a polar crystal (CsBr), which exhibits a strong phonon-polariton (Reststrahlen) resonance in the range 2.2 – 3.3 THz [20]. We simulated the SD-s-SNOM near-field amplitude (s_3) (Fig. 2(a)) and phase (φ_3) signals (Fig. 2(b)) for both CsBr and Au as a function of wave number, using a single phonon oscillator model in the framework of the finite dipole model (see Appendix 2). Our findings show that, although Au exhibits the expected flat amplitude response and negligible phase throughout the THz frequency range investigated, CsBr shows a four-times stronger s_3 peak at 90 cm^{-1}, and a large phase signal $\varphi_3 \approx 150°$ at this wave number. Hence, we prepared a suitable sample comprising a CsBr crystal, coated with a thin (100 nm) Au film, and selected a THz QCL that operated single mode in continuous wave at 90.3 cm^{-1} (2.7 THz). These choices should ensure a strong near-field amplitude and phase contrast at CsBr/Au steps obtained by mechanically scratching the Au thin film to expose the underlying CsBr surface.

Figures 2(c)-2(d) compare the AFM topography (Fig. 2(c)) and the SD-s-SNOM image (Fig. 2(d)) of a CsBr/Au step, simultaneously obtained while raster-scanning in the x-y plane underneath the tip and recording ΔV_3 at each pixel. To show the L dependence of both the ΔV_3 signal and the optical contrast between CsBr and Au, we changed the optical phase ($\omega_0 \frac{2\Delta L}{c}$) over a 2π range in π/3 steps ($\Delta L = 9.25\,\mu m$), every Δy = 0.5 μm during the acquisition. We thus observe 13 striped regions in Fig. 2(d). In order to retrieve amplitude and phase from the collected optical images, each line in Fig. 2(c) and 2(d) were preliminarily horizontally shifted to straighten the CsBr/Au edge. Then the signal ΔV_3 was vertically averaged in each stripe and associated with the corresponding ΔL value. Finally, sinusoidal functions (Eq. (2) were fitted to the $<\Delta V_3>$ vs ΔL curves to extract the amplitude s_3 and phase φ_3 as a function of the horizontal distance from the CsBr/Au edge (Fig. 2(f) and Fig. 2(g)). Then the height (Fig. 2(e)) and the signal ΔV_3 were vertically averaged on each stripe and associated with the corresponding L value. From the steep rise of the optical signal at the edge the Au film on the CsBr crystal, we can estimate the optical spatial resolution. To address the issue we have followed the same procedure detailed for Fig. 1(e). The full-width-at-half-maximum of the Gaussian curves interpolating the derivative function of the amplitude and phase signals (red curves in the insets of Figs. 2(f) and 2(g)), give estimates of the spatial resolutions: 54 nm and 60 nm for the amplitude and phase signals, respectively.

Optics EXPRESS

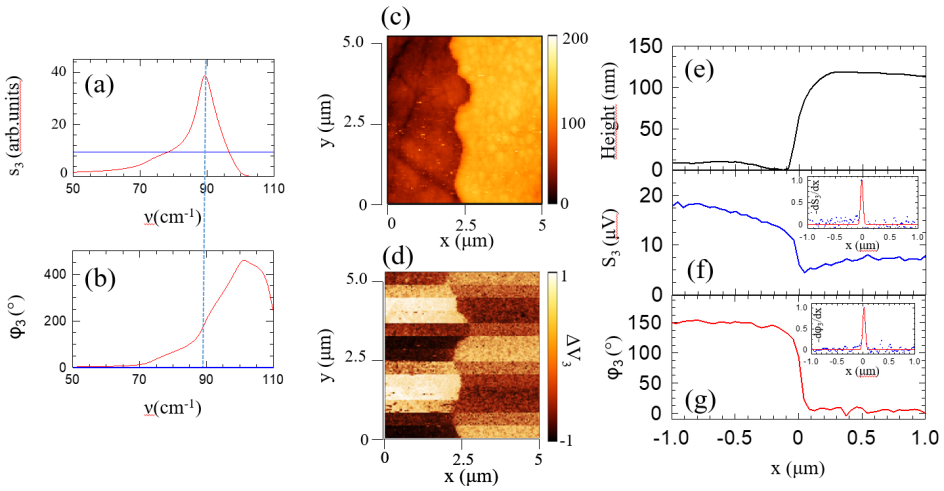

Fig. 2. Amplitude and phase resolved THz nanoscopy on a resonant polar crystal. (a-b) Simulated, near-field resonant dielectric response of CsBr (red lines) and Au (blue lines): amplitude (s_3) and phase (φ_3) plots as a function of wave number. The dashed vertical line corresponds to the probing laser frequency. (c) Atomic force microscope image of a 5 μm x 5.5 μm area of the CsBr/Au sample. Step sizes of $\Delta x = \Delta y = 41.6$ nm were used. (d) Self-detected near field 3rd order signal. Every $\Delta y = 0.5$ μm the PZM mirror position is changed in order to shorten the optical path by $\Delta L = -9.25$ μm. (e-g) average topography (e), amplitude s_3 (f), and phase φ_3 (g) as a function of the position with respect to the CsBr/Au edge. The insets in Figs. 2(f) and 2(g) show the spatial derivative of the amplitude 2(f) and phase 2 (g) signals, which have been fitted by Gaussian functions (red curves) with full-width-at-half-maxima of 54 nm and 60 nm, respectively.

In Fig. 3, we demonstrate the strong sensitivity of SD-s-SNOM to changes in the amplitude and phase of the effective polarizability of the coupled tip-sample system. For this, we exploited the strong dependence of s_3 and φ_3 on the tip sample distance z (see Appendix 2) [21] and recorded ΔV_3 during approach curves obtained by progressively stepping the PZM position by $\Delta L = 9.25$ μm. For each value of z, s_3 (Fig. 3(a)) and φ_3 (Fig. 3(b)) were extracted by fitting sinusoidal functions (Eq. (2) to the ΔV_3 vs L curves. The prevalent near-field nature of 3rd harmonic signals is shown by the monotonic decrease of both the amplitude and phase signals for increasing z, with s_3 becoming negligible and φ_3 saturating for $z > 60$ nm. The approach curves of Fig. 3(a)-3(b) are nicely reproduced by the calculated near-field amplitudes (s_3) (Fig. 3(c)) and phases (φ_3) (Fig. 3(d)) of CsBr and Au, solving the full set of transcendental coupled LK equations, with no approximations, at each experimental L value (see Appendix 2). Similarly, our technique is expected to measure changes of the real and imaginary part of the effective polarizability as a function of the incident laser wavelength.

Optics EXPRESS

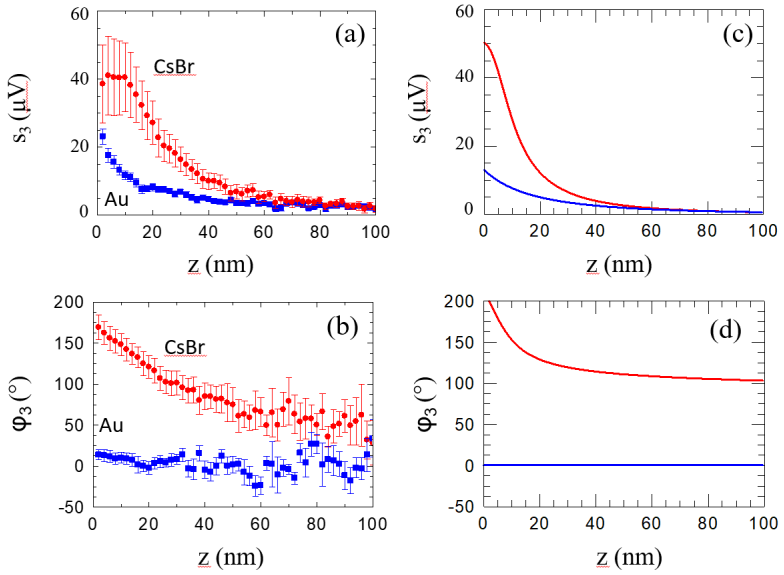

Fig. 3. THz near field amplitude and phase as a function of tip-sample distance (approach curves). (a-b) Comparison between the experimental amplitude (a) and phase (b) of CsBr (red) and Au (blue), collected as a function of the tip-sample distance z, using dither amplitude 106 nm and setting L such that ΔV_3 is maximum at $z = 0$; (c-d) Calculated near-field amplitudes (s_3) (c) and phases (φ_3) (d) of CsBr (red curves) and Au (blue curves) (see Appendix 2).

2.5 Application for 2D material imaging

Finally, we demonstrate the capability of SD-s-SNOM to image doped van der Waals layered materials. We selected black phosphorus (BP), an emerging layered semiconductor, which has been recently demonstrated to be a suitable material system in the THz for photodetectors [22, 23], and near-field optical probes [25]. Here we study BP flakes with different thickness and carrier densities (see the estimate of free carrier density in black phosphorus flakes in Experimental Methods section) that were transferred onto a Si/SiO_2 substrate by mechanical exfoliation [23, 26]. A thin (5 nm) SiO_2 protection layer was deposited via sputtering to encapsulate the material system and avoid degradation under ambient exposure, ensuring that flakes remained clean and stable for several months [22, 23].

Figure 4 compares the topography images (Figs. 4(a), 4(c), and 4(e) and the corresponding ΔV_3 signals (Figs. 4(b), 4(d), and 4(f) collected on Se-doped BP flakes. A near-field contrast is clearly observed between the Se-doped BP-flakes and the SiO_2 substrate in the 2D scans of ΔV_3 shown in Fig. 4(b), 4(d). This effect is also evident in the profile of ΔV_3 measured across the edge of the Se-doped BP flakes (Figs. 4 (l) and 4(m)). In Fig. 4(f) the optical phase was changed at constant steps of $0.39\ \pi$ ($\Delta L = 5.5\,\mu m$), every $\Delta y = 0.21$ μm during the scan.

To extract the amplitude and phase from the optical images, each line in Fig. 4(e) and 4(f) were preliminarily horizontally shifted to straighten the BP/SiO_2 edge, in analogy to the analysis performed on the CsBr/Au sample (Figs. 2(c)-2(g)). Then, the height (Fig. 4(g)) was vertically averaged on each stripe and associated with the corresponding L value. From the striped image of Fig. 4(f) we extracted the near field amplitude s_3 (Fig. 4(h)) and phase φ_3 (Fig. 4(i)) profiles at the BP/SiO_2 step edge. Apparently, no phase contrast between BP and SiO_2 is observed, due to the off-resonance excitation of both materials, as expected since in both cases optical phonon resonances fall in the mid-IR [27]. Incidentally, the detected near-field scan results highly sensitive to the presence of oxidation-induced clusters on the surface of the investigated BP flake, which causes an abrupt change of the detected optical signal.

Optics EXPRESS

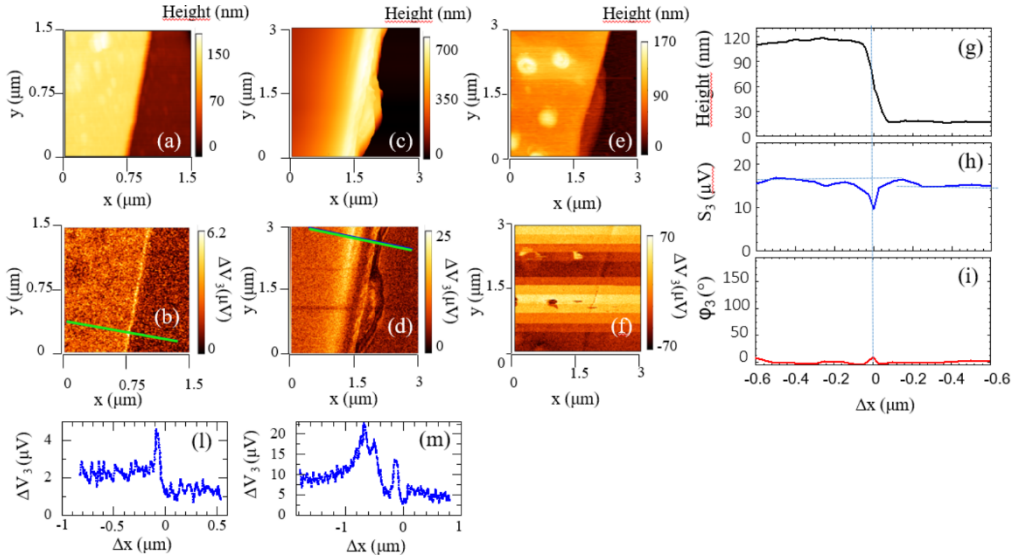

Fig. 4. SD s-SNOM nanoscopy at THz frequencies of doped black-phosphorus. (a, c, e) AFM tomographic images and (b, d, f) corresponding ΔV_3 near field optical signal collected on a set of representative Se-doped BP flakes having thickness 130 nm (a), 300 nm (c) 100 nm (e); (f) Self- detected near field 3rd order signal. Every Δy = 0.21 μm the PZM mirror position is changed in order to shorten the optical path by ΔL = 5.5 μm. (g-i) average topography (g), amplitude s_3 (h), and phase φ_3 (i) as a function of the position with respect to the Se-doped BP/SiO_2 edge. The sharp features in panels (h) and (i) at Δx = 0 are known edge artifacts arising at the sharp edges of the mechanical exfoliated black phosphorus flakes. The dashed vertical line in panels (h-i) corresponds to the BP/SiO_2 edge. The horizontal dashed lines in panel (g) mark the amplitude contrast between the two materials. (l-m) ΔV_3 profiles averaged over seven adjacent rows of pixels along the green lines in panels (b) and (d), respectively

3. Conclusion

In conclusion, we have demonstrated a detector-less s-SNOM system operating at THz frequencies that provides both amplitude and phase contrast with deep sub-wavelength (60-70 nm) in-plane spatial resolutions. These achievements are expected to have a profound impact on the flourishing field of QCL-based THz imaging, in which near-field coherent detection has been missing, so far. The ability of SD-s-SNOM to resolve both the amplitude and phase of the THz field opens up the possibility of mapping the complex permittivity of a target using QCLs with a high spatial resolution, down to a few tens of nanometers. The proved sensitivity to thin-layered samples of our novel THz SD s-SNOM opens the way to further investigations of resonant 2D-materials and combined Van der Waals heterostructures, with potential impacts in plasmonics and optoelectronics.

Future experiments could make use of the tunable bandgap of BP [28] to control its mode-activation energy as well as exploiting resonant excitation to retrieve plasmonic features. The in-plane asymmetry of BP [29] may also allow for further tunability. Looking forward, complex heterostructures that combine BP with graphene, transition-metal dichalcogenides and hexagonal boron nitride have the potential to provide a robust technological platform for THz nanophotonics and ultrafast plasmonics.

Further development of SD-s-SNOM will also benefit from the availability of broadly tunable THz QCLs [30] and THz QCL combs [31, 32]. Also, the inherent ultrafast response of QCLs to optical feedback perturbations, associated with their unipolar nature and the ps-long lifetimes of inter-subband transitions, raises a compelling perspective for new time-resolved hyper spectral THz imaging systems with deep sub-wavelength spatial resolutions (< 100 nm or λ/1000).

Optics EXPRESS

The unique features of SD-s-SNOM, i.e. the inherent field sensitivity and compactness, can in principle lead to further elimination of intermediate optical elements and true access to near-field radiation, opening the way to many applications in fields ranging from biosensing to quantum optics [33]. Also, a full integration of sample and nanoscopy set-up inside the same cryostat may become possible, thereby allowing to exploit in situ the potential of coherent THz nanoscopy at cryogenic temperatures and under high magnetic fields, for understanding fundamental excitations, such as phonons, magnons, polaritons, and phase transitions in exotic semiconductor and organic nanostructures, superconductors, multiferroics, and metamaterials, just to mention a few examples.

Appendix 1

Experimental arrangement

A bound-to-continuum single longitudinal mode THz QCL emitting, at a wavelength λ = 111 μm (2.7 THz, 90.3 cm^{-1}) with a surface plasmon waveguide, was grown by molecular beam epitaxy employing a GaAs/$Al_{0.15}Ga_{0.85}As$ heterostructure on a nominally undoped GaAs substrate. The 10-μm-thick active region was embedded between a doped ([Si] = 3.0 × 10^{18} cm^{-3}) 700-nm-thick GaAs bottom layer, and a doped ([Si] = 5.0 × 10^{18} cm^{-3}) 200-nm-thick GaAs top contact layer. The GaAs semi-insulating substrate was lapped down to a thickness of 150 μm. Laser bars 1.5 mm long and 150 μm wide were cleaved and mounted on a copper bar.

The QCL was mounted in a liquid helium continuous-flow cryostat fitted with a polymethylpentene window, and maintained at a fixed heat sink temperature of 15 K. To maximize the sensitivity to coherent optical feedback [14, 15], the QCL was driven in continuous wave at a current I = 450 mA (J = 132 A/cm^2) which is just 5% higher than the threshold current density (J_{th} = 125A/cm^2), using a highly stable current generator (Lightwave Electronics, mod. QCL 2000). The emitted THz beam was collimated using a 90° off-axis parabolic mirror with an effective focal length of 50 mm, and reflected by a mirror mounted on a piezo-controlled translator stage into the entrance optical port of a commercial near-field microscope (Mod. NeaSNOM, Neaspec, Martinsried, Germany). A 5 dB substrate-free, metal-mesh diffractive attenuator (Mod. 224, Lasnix, Berg, Germany) was placed in the beam. In the microscope, a second paraboloid mirror with an equivalent focal length of 25 mm focused the beam onto a Pt tip (Bruker, mod. RMN-25PT300) having a nominal apex radius of 50 nm, a shank length of 80 μm, and which was sinusoidally dithered at its resonant frequency Ω = 15380 Hz. The laser polarization lay in the plane containing the tip in order to induce an oscillating dipole in the tip efficiently. The average optical path length from the QCL front facet to the tip was $L \approx 60$ cm. The scattered radiation was collected by the same focusing paraboloid mirror and coupled back into the laser cavity along the same incident optical path. The voltage modulation across the QCL terminals produced by the self-mixing effect was pre-amplified using a low-noise amplifier (DL Instruments, mod. 1201) and demodulated up to the highest harmonic order (n = 5) allowed by the electronic card of the NeaSNOM.

The density of free carriers n_e in the black phosphorus samples was estimated by performing transport analysis on field effect transistors FET having flakes with identical thickness as active channels [20–22, 24, 25]. n_e is connected with the FET threshold voltage V_{th} via the relation $n_e = \frac{C_G \Delta V_{th}}{q A_G}$, where C_G is the gate-to channel capacitance, A_G the gated BP area, and q is the electron charge. We measured $n_e \approx 4.0 \times 10^{17}$ cm^{-3} for the flake shown in Figs 4(a)-4(b), $n_e \approx 7.0 \times 10^{17}$ cm^{-3} for the flake shown in Figs. 4(c)-4(d) and $n_e \approx 1.5 \times 10^{17}$ cm^{-3} for the flake shown in Figs. 4(e)-4(f).

Optics EXPRESS

Appendix 2

Theory of self-detection scattering-type scanning near-field optical microscopy (SD s-SNOM)

The near-field scattering is modeled according to the finite-dipole model, in which the tip, described as a spheroid having an effective length L_t and apex radius a, polarizes the sample. The latter, in turn, acts back on the tip, yielding a near-field interaction specific to the sample material. The radiation scattered by a tip, placed with its apex at a distance z from a target surface, is proportional to the effective polarizability α_{eff} and can be written as $\sigma = \frac{E_s}{E_i} \propto (1+r_p)^2\ \alpha_{eff}$, where [34]

$$\alpha_{eff} = a^2 L_t \frac{L_t(\epsilon_t - 1)(2L_t\sqrt{1-\frac{a}{L_t}} + a\ln\frac{\left(1-\sqrt{1-\frac{a}{L_t}}\right)^2}{\frac{a}{L_t}})}{2L_t\sqrt{1-\frac{a}{L_t}}\,(L_t - a\epsilon_t) - aL_t(\epsilon_t - 1)ln\frac{\left(1-\sqrt{1-\frac{a}{LL_t}}\right)^2}{\frac{Ra}{L_t}}} \cdot (2 + \frac{\beta\left(g\frac{a+z}{LL_t}\right)\ln\left(\frac{4L_t}{4z+2a}\right)}{\ln\left(\frac{4L_t}{a}\right) - \beta\left(g - \frac{3a+4z}{4L_t}\right)\ln\left(\frac{2L_t}{2z+a}\right)}). \quad (3)$$

Here, E_i and E_s are the incident and scattered fields, respectively, and r_p is the far-field Fresnel reflection coefficient for p-polarized incidence. The sample dielectric permittivity ε_s enters through the so-called surface response function $\beta = (\varepsilon_s - 1) / (\varepsilon_s + 1)$, and ε_t is the tip dielectric function. The apex-sample surface distance z oscillates with frequency Ω and amplitude $2z_A$ as $z(t) = z_A + z_A\cos(\Omega t)$; g, is a complex factor related to the fraction of the total charge induced in the spheroid.

The complex effective scattering efficiency is represented in terms of amplitude and phase as $\sigma\ (t) = s(t)e^{i\varphi(t)}$, where both s and φ show a nonlinear dependence as a function of z. We have found a good agreement with the experimental results by using the values L_t = 530 nm, and $g = 0.98e^{0.08i}$.

Coherent optical feedback in a semiconductor laser cavity is described by the Lang-Kobayashi (LK) model [14, 15, 35], in which two coupled differential equations describe the evolution of the excited state population *N(t)* and the optical field *E(t)*. The crucial feedback contribution in this model is provided by an additive term, representing the retarded field re-entering the laser cavity.

The LK equations read [35]:

$$\frac{dE(t)}{dt} = \frac{1}{2}(1+i\alpha_H)\left[G_n\left(N(t)-N_0\right) - \frac{1}{\tau_p}\right]E(t) + \frac{\gamma}{\tau_c}E(t-\tau)e^{-i\omega_0\tau}$$
$$\frac{dN(t)}{dt} = \frac{J\eta}{qd} - \frac{N(t)}{\tau_e} - G_n\left(N(t)-N_0\right)\left|E(t)\right|^2 \quad (4)$$

where N_0 is the carrier density at transparency, G_n is the gain coefficient, $\tau = 2L/c$, τ_p = 30 ns and τ_c = 35 ns are the photon life time and the cavity round trip time inside the QCL cavity, respectively, and τ_e is the carriers decay time ($1-10\,ps$), J is the current density, η is the internal quantum efficiency, d is the active layer thickness and q is the electron charge, γ is the feedback strength parameter, i.e. the fraction of the back-scattered field that efficiently

Optics EXPRESS

couples with the lasing mode. A value $\alpha_H = 1.5$ for the linewidth enhancement factor was used, which is appropriate for a THz QCL close to threshold [36, 37].

In our theoretical approach, we consider a feedback field provided only by the tip-scattered field E_s and neglect any contribution from the background field. The latter is a component well-known in s-SNOM that can be experimentally suppressed by recording signals at higher harmonics of Ω. Considering that the feedback path $2L$ depends on the oscillating tip position, we assume:

$$\gamma(t) \propto \sigma(t) = s(t)e^{i\varphi(t)} = \sum_{n=-\infty}^{+\infty} \sigma_n e^{in\Omega t} = \sum_{n=-\infty}^{+\infty} s_n e^{i\varphi_n} e^{in\Omega t}. \quad (5)$$

The optical feedback coefficient C is defined as $C = |\gamma|\sqrt{1+\alpha_H^2}\,\frac{2L}{c\tau_c}$. In the very weak feedback limit, when $C \approx 10^{-2}$, as appropriate under our experimental condition, the perturbation induced on the laser frequency can be neglected and one can assume that the frequency of the retro-injected laser coincides with ω_0, radically simplifying the self-mixing formalism [14–16]. In fact, the sinusoidal line shapes unveiled in the experiments of Fig. 1 confirm that the system is in the very weak feedback self-mixing regime [19], with estimated values of the feedback coefficient $C \approx 0.03 - 0.1$. Hence, the LK equations are solved for the steady-state value of the carrier variation ΔN induced by the self-mixing (with respect to the free running laser value at threshold), assuming the tip and the PZM dynamics are slow with respect to field and carrier timescales:

$$\Delta N = -2|\gamma|\frac{\tau_p}{\tau_c}\cos(\omega_0 \frac{2L(t)}{c} - \varphi(t)) \quad (6)$$

noting that ΔV is proportional to ΔN [16], we find the following expression:

$$\Delta V(t) \propto s(t)\cos(\omega_0 \frac{2L(t)}{c} - \varphi(t)) \quad (7)$$

Due to the tip oscillation, the laser-tip distance varies as $L(t) = L_0 + 2z_A - z(t)$, where $L_0 + 2z_A$ is the laser-target distance which may vary, if the PZM is moved, on time scales much longer than the tip period $2\pi/\Omega$.. Moreover, we approximate $L \approx L_0$ in the following, since in our experimental configuration $z_A \ll \lambda$.

By introducing the spectral representation of the scattered amplitude in Eq. (4), we can rewrite the steady state equations accordingly, where the RHS term of Eq. (7) becomes:

$$\begin{aligned}
&\Delta V(t) \propto \sum_{n=-\infty}^{+\infty} S_n \cos\left(\omega_0 \frac{2L}{c} - \varphi_n - \Omega_n t\right) \\
&= \sum_{n=0}^{\infty}\left[s_n \cos\left(\omega_0 \frac{2L}{c} - \varphi_n - \Omega_n t\right) + s_{-n}\cos\left(\omega_0 \frac{2L}{c} - \varphi_{-n} + \Omega_n t\right)\right] - s_0 \cos\left(\omega_0 \frac{2L}{c} - \varphi_0\right) = \sum_{n=0}^{\infty} S_n \left[\cos\left(\omega_0 \frac{2L}{c} - \varphi_n - \Omega_n t\right) + \cos\left(\omega_0 \frac{2L}{c} - \varphi_n + \Omega_n t\right)\right] - s_0 \cos\left(\omega_0 \frac{2L}{c} - \varphi_0\right) \\
&= \sum_{n=0}^{\infty} 2 s_n \left[\cos\left(\omega_0 \frac{2L}{c} - \varphi_n\right)\cos(\Omega_n t)\right] - s_0 \cos\left(\omega_0 \frac{2L}{c} - \varphi_0\right)
\end{aligned} \quad (8)$$

where $\Omega_n = n\Omega$, and $s_n = s_{-n}$, since ΔV is an even function of time (ΔV depends on time only through z). Equation (8) allows information retrieval on the medium optical response since it provides the link between the demodulated SMI signal and the phase and amplitude spectral components of the scattering amplitude σ.

$$\Delta V_n \propto s_n \cos(\omega_0 \frac{2L}{c} - \varphi_n). \quad (9)$$

The simulated plots presented in Figs. 2(a)-2(b) and 3(c)-3(d) have been obtained by solving in steady state Eq. (7) in the case of moving mirror PZM, assuming a total

Optics EXPRESS

displacement ΔL of three interferometric fringes, where each fringe is $\frac{\lambda}{2} \approx 55.5\,\mu m$ corresponding to a phase shift $\frac{\omega_0 2\Delta L}{c} = 2\pi$ (Fig. 1). The oscillating laser voltage ΔV is then processed with a fast Fourier transform algorithm (equivalent to the lock-in filtering in the experiment) to recover the components ΔV_n corresponding to each mirror displacement. The amplitude and phase values s_n and φ_n, n = 1...5, are finally extracted by a fitting procedure based on Eq. (9).

Funding

EU Graphene Flagship. M.S.V. acknowledges support from the European Union ERC Consolidator Grant SPRINT and from the second half of the Balzan Prize 2016 in applied photonics delivered to Federico Capasso. G.S. acknowledges support from PON SISTEMA (MIUR). A.G.D., E.H.L., and L.H.L. acknowledge support from the EPSRC (UK) (EP/J017671/1, EP/P021859/1), and from the Royal Society and Wolfson Foundation. R.H. acknowledges support from the Spanish Ministry of Economy and Competitiveness (National plan MAT2015-65525-R).